JOURNAL OF GEOPHYSICAL RESEARCH: SPACE PHYSICS, VOL. 118, 1306–1318, doi:10.1002/jgra.50196, 2013

Kinetic simulations of 3-D Farley-Buneman turbulence and anomalous electron heating

M. M. Oppenheim[1] and Y. S. Dimant[1]

Received 30 November 2012; revised 4 February 2013; accepted 22 February 2013; published 28 March 2013.

[1] Electric fields map from the magnetosphere to the *E* region ionosphere where they drive the intense currents of the auroral electrojet. Particularly during geomagnetic storms and substorms, these currents become sufficiently intense to develop Farley-Buneman (FB) streaming instabilities and become turbulent. This leads to anomalous electron heating which can raise the electron temperature from 300 K to as much as 4000 K and, also, modifies auroral conductivities. This paper describes the first fully kinetic 3-D simulations of electric field-driven turbulence in the electrojet and compares the results with 2-D simulations and observations. These simulations show that 3-D turbulence can dramatically elevate electron temperatures, enough to explain the observed heating. They also show the saturated amplitude of the waves; coupling between linearly growing modes and damped modes; the propagation of the dominant modes at phase velocities near the acoustic velocity, slower than in 2-D simulations; and anomalous cross-field electron transport, leading to a greatly increased *E* region Pedersen conductivity. These simulations provide information useful in accurately modeling FB turbulence and represent significant progress in understanding the electrojet.

Citation: Oppenheim, M. M., and Y. S. Dimant (2013), Kinetic simulations of 3-D Farley-Buneman turbulence and anomalous electron heating, *J. Geophys. Res. Space Physics*, *118*, 1306–1318, doi:10.1002/jgra.50196.

1. Introduction

[2] Large-scale currents and electric fields propagate from the magnetosphere into the auroral *E* region ionosphere where they drive electron drifts that, upon reaching a sufficient amplitude, create plasma instabilities and turbulence. These cause density irregularities, anomalous electron heating (AEH), and conductivity changes. While these phenomena have been studied experimentally and theoretically for six decades, only in the last decades have numerical simulations become useful. The first simulations to explore the nonlinear behavior of *E* region instabilities were limited to the 2-D plane perpendicular to the geomagnetic field $\vec{B}_0$. Today, taking advantage of modern, massively parallel, supercomputers, we can resolve over 1 billion wave modes (8192 along $\vec{B}_0$ by 512 × 512 perpendicular to $\vec{B}_0$) in fully 3-D kinetic simulations.

[3] This study uses the massively parallel particle-in-cell (PIC) simulator, EPPIC, first discussed in *Oppenheim et al.* [2008]. This code models both electrons and ions as PIC particles, capturing the kinetic and thermal behavior of both these species. These simulations explored a range of parameters intended to model the auroral *E* region for a span of altitudes between 100 and 110 km.

[4] These simulations demonstrate conclusively that 3-D Farley-Buneman (FB) turbulence causes anomalous electron heating (AEH). For a 3-D simulation mimicking parameters at 109 km altitude, driven by 105 mV/m, the electron temperature climbed from a few hundred Kelvin to a sustained 2000 K, while a similar simulation for 106 km reached and maintained 1500 K. While these simulations do not exactly model the parameters found in the ionosphere, they do show that 3-D FB turbulence produces far more electron heating than an equivalent 2-D turbulence and also allows us to quantify the AEH and understand its origin.

[5] Anomalous electron heating is important because it modifies ionospheric conductances and therefore affects the coupling between the magnetosphere and ionosphere. It does this by reducing the local plasma recombination rate, which causes a gradual elevation of the mean plasma density [*Gurevich*, 1978; *St.-Maurice*, 1990; *Dimant and Milikh*, 2003; *Milikh and Dimant*, 2003; *Milikh et al.*, 2006]. The elevated plasma density increases both the Hall and Pedersen conductivities in proportion. However, this mechanism requires tens of seconds or even minutes because of the slow development of the ionization-recombination equilibrium. Although these simulations do develop the requisite temperatures to trigger this recombination, they not reach this time scale.

[6] Electrojet turbulence instantaneously modifies Pedersen ionospheric conductances through the mechanism of wave-driven nonlinear currents [*Oppenheim*, 1997;

[1]Center for Space Physics, Boston University, Boston, Massachusetts, USA.

Corresponding author: M. M. Oppenheim, Center for Space Physics, Boston University, 725 Commonwealth Ave., Boston, MA 02461, USA. (meerso@bu.edu)

2169-9380/13/10.1002/jgra.50196

Buchert et al., 2006; *Dimant and Oppenheim*, 2011a]. This current develops when the wave-generated electric field causes electrons to $\vec{E} \times \vec{B}$ drift in one direction along the crest of each wave and in the opposite direction along the depletion of the wave. Due to the higher plasma densities at the crests of the waves than in the depletions, a net current flows perpendicular to the direction of the wave propagation. This nonlinear current, $\vec{J}_{\mathrm{NC}}$, is intimately related to AEH: the total energy deposited per unit time on all anomalous heating processes equals the "turbulent" Joule heating, $\vec{J}_{\mathrm{NC}} \cdot \vec{E}_0$. The simulations show that these nonlinear currents (NC) exceed the laminar ion Pedersen current by as much as 80%. They also show that both the NC and the AEH differ dramatically in 2-D and 3-D, in agreement with the earlier theoretical predictions discussed in *Dimant and Oppenheim* [2011a, 2011b].

[7] These simulations reproduce many aspects of the electrojet radar data. In particular, the saturated spectra of 3-D FB turbulence generated by these simulations follow a cosine dependence with respect to flow angle, as in 2-D. Also, in 3-D the phase velocity of the most energetic modes lies well below the 2-D phase velocity and close to the highest estimates of the acoustic velocity.

2. Background

[8] Plasma irregularities in the *E*-region ionosphere were first detected shortly after the invention of radar in the 1940s, and detailed radar studies of this phenomenon began in the 1950s [*Bowles*, 1954]. Since then hundreds of studies, both experimental and theoretical, have been undertaken to further our understanding of the origin, evolution, and effects of *E*-region irregularities. These studies have been reported on in hundreds of papers and a number of books [*Fejer et al.*, 1984; *Farley*, 1985; *Kelley*, 2009]. In the last 15 years, simulations have become a useful tool for exploring the nonlinear evolution of *E*-region waves. For a general discussion of background material appropriate to this paper, please refer to *Oppenheim and Dimant* [2004] and *Oppenheim et al.* [2008]. In this paper, we will limit our discussion of background to material that has appeared in the last few years.

[9] On the experimental side, there has been a concerted effort over the last decade to simultaneously use multiple frequency radars, imaging radars, and Faraday rotation to study electrojet turbulence at the Jicamarca Radio Observatory [*Hysell et al.*, 2007]. They found structuring of the system at the 3–5 km scale size and east-west asymmetries which may be explained by thermal effects [*Dimant and Oppenheim*, 2004]. *Woodman and Chau* [2002] and *Hysell et al.* [2007] present compelling evidence that the phase velocities of the waves go as $C_s \cos\theta$ where C_s is an estimate of the ion acoustic speed and θ is the angle between the direction of the fastest waves and the measured wave.

[10] A number of theories have been advanced to better explain the behavior of Farley-Buneman (FB) turbulence in the last decade. *Otani and Oppenheim* [2006] further developed the theory of three or four mode coupling mechanisms of saturation [*Sahr and Farley*, 1995; *Dimant*, 2000; *Hamza and Imamura*, 2001]. This paper shows how a FB system limited to very few modes will saturate and show behavior such as density perturbation levels and phase velocities which match observations quite nicely. They also show how mode-coupled systems have constraints on phase velocities and wave directions. However, these systems never resemble the fully turbulent simulations that include diffusive and kinetic effects neglected in the mode coupling models. *Hysell and Drexler* [2006] further developed the nonspectral "blob" approach to modeling the saturated FB system [*St.-Maurice and Hamza*, 2001], showing how the blobs rotate and distort. While these models show some interesting aspects of nonlinear dynamics of FB turbulence, they also exclude diffusion and kinetic effects. The net result is that the "blob" models do not resemble the simulated FB turbulence. Finally, there have been a number of recent papers commenting on interesting aspects of FB turbulence. *Haldoupis et al.* [2005] look at the role of density gradients on FB waves. *Bahcivan and Cosgrove* [2010] discuss the effect of vertical electron density gradients in the auroral regions on FB turbulence. None of these studies address the fully 3-D turbulence and the resulting anomalous electron heating (AEH).

[11] Small-scale fluctuations generated by FB instabilities can cause enormous AEH. For about 30 years, radars have observed strong electron temperature elevations from 300–500 K up to more than 4000 K, correlating with strong convection fields $\vec{E}_0$ [*Schlegel and St.-Maurice*, 1981; *Providakes et al.*, 1988; *Stauning and Olesen*, 1989; *St.-Maurice et al.*, 1990; *Williams et al.*, 1992; *Foster and Erickson*, 2000; *Bahcivan*, 2007]. Simple estimates show that regular ohmic heating by $\vec{E}_0$ alone cannot account for such huge temperature elevations. A strong correlation between AEH and E_0, as well as theoretical arguments, provide evidence that the FB-generated turbulent electric fields causes AEH [*St.-Maurice and Laher*, 1985; *Robinson*, 1986; *Robinson and Honary*, 1993; *Providakes et al*., 1988; *St.-Maurice*, 1987; *St.-Maurice*, 1990; *Dimant and Milikh*, 2003; *Bahcivan et al*., 2006; *Bahcivan et al*., 2012]. These theories argue that AEH occurs largely because the turbulent electrostatic field, $\delta\vec{E}$, has a small component $\delta E_{\parallel}$ parallel to the geomagnetic field $\vec{B}_0$. The importance of $\delta\vec{E}_{\parallel}$ makes the entire process fully 3-D, precisely what these simulations explore.

3. Simulation Methods and Limitations

[12] To study the growth, evolution, and saturation of *E*-region waves, we use the Electrostatic Parallel Particle-in-Cell simulator EPPIC to follow the dynamics of a collection of ions and electrons as they respond to both external and internally generated electric fields in full 3-D. *Oppenheim et al.* [2008] describe the techniques applied by this simulator, and *Oppenheim and Dimant* [2004] discuss many of its limitations, although both of these focused on 2-D simulations. The 3-D simulations in this paper apply this same simulator on a considerably larger scale, running on the Kraken supercomputer, using just over 8000 processors simultaneously. We believe the resulting simulations present the most physically accurate simulations of field-driven electrojet turbulence yet performed.

[13] The dominant computational cost of these simulations results from tracking electrons as they gyrate. To reduce this expense, we use an electron mass which is 44 times more massive than the physical electron mass, making the ion-to-electron mass ratio close to that found in a

H^+ plasma. For *Oppenheim et al.* [2008], we performed a series of 2-D tests to demonstrate that this elevated electron mass has little effect on these simulations by comparing a run with $m_e^{\text{sim}} = 44m_e$ to one with $m_e^{\text{sim}} = 6m_e$. In 3-D, the electron mass also determines the aspect angle, $\Theta_0 \equiv [m_e\nu_e/(m_i\nu_i)]^{1/2}$, which approximates the largest angle between a wavevector and perpendicular to $\vec{B}$ at which linearly unstable modes persist. Raising the electron mass increases Θ_0, reducing the number of modes parallel to $\vec{B}$ the simulation must resolve. This allows for a smaller, less expensive 3-D simulation. However, a higher m_e^{sim} also requires a proportionately reduced ν_e, and, if ν_e falls below ν_i, then the behavior of FB waves changes substantially. An otherwise identical simulation shows that if $m_e^{\text{sim}} = 88m_e$, then the saturation amplitude increases, and the heating diminishes. A very expensive simulation with $m_e^{\text{sim}} = 22m_e$ and a longer box along $\vec{B}_0$ showed results similar to the $m_e^{\text{sim}} = 44m_e$ ones used in this study.

[14] The simulations presented in this work have a number of things in common: They use periodic boundary conditions in all directions. This means that the top of the simulation box connects to the bottom, the right to the left, and the front to the back. This method allows us to use a rapid spectral technique to determine the field from Poisson's equation. Periodic simulations allow only a limited number of wave modes and prevent all others. This means that modes which span the entire simulation box or only a few grid cells will generally be poorly represented. These simulations, though, do represent millions of modes accurately.

[15] These runs initially position the particles uniformly through the simulation space and assigns initial velocities to make the particle distribution Maxwellian. As a result of the discreteness of the particles, an initial, nonzero noise level exists which substantially exceeds that found in nature. We do not seed these simulations with any initial perturbation, instead letting the instability grow from noise. We require that the total averaged electric field $\langle E^2 \rangle$ of the saturated state waves exceeds the initial noise by at least one order of magnitude. This means we must have at least a few hundred particles per cell. We achieve this by using just over 8000 CPUs simultaneously.

[16] These simulations use an elastic collision algorithm where at each time step all charged particles have a probability of colliding with a neutral particle using one of three elastic scattering algorithms: A constant cross-section model sets the probability of collision proportional to the difference between the charged and a randomly generated neutral-particle velocities; a Maxwell-molecule model makes the probability of collision independent of the velocities; and, lastly, EPPIC includes a model making the collision rate proportional to the energy $(\propto \mathrm{v}_e^2)$ useful for modeling electron-N_2 collisions.

[17] In the *E* region, inelastic electron collisions dominate over elastic ones. In order to simulate this, EPPIC has the PIC electrons collide with neutrals with a smaller mass than real atmospheric neutrals. Also, to best recreate the $\nu_e \propto \mathrm{v}_e^{5/3} \propto T_e^{5/6}$ described in *Gurevich* [1978], the simulated electrons collide at a rate proportional to v_e^2 [*Dimant and Sudan*, 1995]. Interestingly, over the energy range of interest, $\sim$ 0.03 to 0.3 eV, this actually matches quantum collision calculations more accurately than does $\mathrm{v}_e^{5/3}$. Combining the effective lower neutral mass with a $\nu_e \propto \mathrm{v}_e^2$ mimics electron inelastic collision and heat transfer rates with reasonable accuracy [*Oppenheim et al.*, 2008].

[18] The collision algorithm where $\nu \propto \mathrm{v}$, used for ions, works by selecting a subsample of particles and then comparing the ratio of each particle's velocity to a selected maximum velocity, $\mathrm{v}_{\mathrm{cmax}}$, to a random number between 0 and 1. If the random number is less than this ratio, then the particle will collide with a neutral; otherwise, it will not. This gives the effect of a constant cross-section particle and a collision rate proportional to the velocity. A weakness of this algorithm arises if the thermal velocity of the colliding distribution becomes more than a small fraction of maximum $\mathrm{v}_{\mathrm{cmax}}$, then the faster particles will always collide, meaning that the constant cross-section collision rate is lost. If $\mathrm{v}_{\mathrm{cmax}}$ is set very high, then the cost of the collision algorithm becomes excessive as large numbers of particles must be tested to obtain a sufficient number to maintain the required collision rate. The value or $\mathrm{v}_{\mathrm{cmax}}$ chosen was a compromise between numerical efficiency and simulation accuracy.

[19] The $\nu, \propto \mathrm{v}^2 \sim T$ collision algorithm works by comparing the random number to the ratio $\mathrm{v}/\mathrm{v}_{\mathrm{cmax}}$ squared. The Maxwell-molecule algorithm simply collides randomly selected particles with no concern for their velocity.

[20] The FB instability and its dominant nonlinearities do not depend on plasma density, only the normalized density gradients $\vec{\nabla}n/n$. Hence, we can use a low density to maximize the Debye length, the smallest scale the grid must resolve. However, as *Rosenberg and Chow* [1998] pointed out, if the density drops too low, the plasma will not maintain quasineutrality. Therefore, the simulation must have $\omega_{pi:sim}/\nu_{i:sim} > 1$ where $\omega_{pi:sim}$ is the simulation ion plasma frequency. Violating this condition will preclude the FB instability.

4. Simulation Results

[21] The paper will focus on a 3-D baseline simulation, a comparison run with halved collision rates, and a set of 2-D simulations with matching parameters. Table 1 lists many of the parameters used for these simulations. As demonstrated below, these simulations have parameters which match those at 106 and 109 km altitude in the auroral zone.

[22] Kinetic distortions of distribution functions make it difficult to estimate accurate fluid collision rates and, hence, effective altitudes from a PIC simulation. To obtain these values, we ran a series of modest-sized (256 processor) simulations with the electric field reduced to 20 mV/m or less, below the FB threshold, eliminating waves and reducing heating to a few degrees. The resulting Pedersen drift rates can then be used to infer the ion-neutral collision rates with high precision from the unmagnetized drift equation, $\hat{\mathrm{v}}_{ix} = (E_{0y}e/m_i)/\nu_i$, where the simulation gives us the average velocity $\hat{\mathrm{v}}_{ix}$. This yields $\nu_i = 1875\ \mathrm{s}^{-1}$ with variances less than $1\ \mathrm{s}^{-1}$.

[23] Obtaining the electron collision rates from the Pedersen drifts requires extracting an average speed of less than 1 m/s from a population where the RMS particle speed exceeds 7 km/s. Instead, we performed another special run,

Table 1. Parameters of Baseline Simulation[a]

Parameter	*B1* Value	Units
grid ($nx \parallel \vec{B}_0 \times ny \times nz$)	$2048 \times 512 \times 512$	
grid size ($dx \times dy \times dy$)	$0.15 \times 0.15 \times 0.15$	m
Δt	3.5×10^{-6}	s
$\vec{B}_0$	$0.5\hat{x}$	Gauss
$\vec{E}_0$	$0.105\hat{y}$	V/m
n_0	4×10^8	$1/m^{-3}$
m_i	5×10^{-26}	kg
m_i/m_e	625	
T_n	300	K
N_e^{pic}	$2. \times 10^9$	
N_i^{pic}	$17. \times 10^9$	
ν_e	297	1/s
ν_i	314	1/s
Ψ	0.003	
Altitude (high latitude)	$\sim$ 106	km

[a]The collision rates, Ψ, and altitude derive from special test simulations as discussed in the text. $\Psi \equiv \nu_e\nu_i/\Omega_e\Omega_i$ and N_e^{pic}, N_i^{pic} are the number of macro PIC particles used to model the behavior of the $n_0 n_x d_x n_y d_y$ particles per length. The T_n is the neutral temperature. All other parameters have their typical meanings.

with an externally imposed $E_\parallel = 0.1$ mV/m, and obtained a collision rate from the relation $\vec{V}_{e\parallel} = -e\vec{E}_\parallel/(m_e\nu_e)$. Since any $E_\parallel$ can heat and distort the electron thermal distribution, we ran a series of test cases to insure that we obtained an accurate collision rate.

[24] The combined ion and electron collision rates tell us the simulated altitude in the electrojet. Calculating $\Psi = \Omega_e\Omega_i/(\nu_e\nu_i)$ and using Figure 2 of *Dimant and Oppenheim* [2004], we see that for *B2*, $\Psi = 0.003$, which corresponds to an altitude of about 115 km. The equivalent altitude at the equator is 120 km.

[25] These parameters create another simulation weakness: the ratio of $\nu_e/\nu_i \approx 1$, while in nature this ratio is about 10. The electron collision rate must drop as we raise the artificial electron-ion mass ratio. As discussed in *Oppenheim et al.* [2008], we can safely raise this mass until $m_{es} \approx 50m_e$.

[26] Accurately modeling ion collisions in the *E* region presents a serious challenge. Simulations run with $\nu_i \propto v_i^2$, $\nu_i \propto v_i$, or a constant ν_i shows that having a collision rate proportional to v_i or v_i^2 does not change the solution by more than a few percent. However, using a constant ν_i leads to a much hotter ion population which raises the FB instability threshold dramatically. The correct collision rate lies somewhere between a $\nu_i \propto v_i$ and constant. As a practical measure, we used $\nu_i \propto v_i$. An equivalent simulation with Maxwell molecules would require an enhanced driving E-field and would have a considerably hotter ion population as the fastest ions collide at the same rates as the far more common slow ones. This type of collision model probably applies to the slower ions but breaks down for the hotter ones.

4.1. Baseline 3-D Simulation Results

[27] Both baseline simulations spanned 307.2 by 76.8 by 76.8 m with parameters mimicking the auroral *E* region. The neutral temperature used for this run was $T_n = 300$ K, somewhat on the cold side of the expected values. However, the plasma quickly heats up due to ohmic heating resulting from the strong—but not absurd—driving field of 105 mV/m.

[28] One can track the growth and saturation behavior of plasma waves by evaluating the total energy stored in the perturbed electric field. Figure 1 shows this for the baseline 3-D and 2-D cases plus the reduced collision rate case and, lastly, a larger 2-D baseline case.

[29] The amplitude of the turbulent $\langle E^2 \rangle$ reaches similar levels in both 3-D and 2-D. By averaging $\langle \delta E^2 \rangle$ over the second half of the 3-D baseline run, we get 160 mV/m, while the 2-D case exceeds this only by a few millivolts per meter. This exceeds the driving electric field of 105 mV/m by 52%, representing a surprisingly large average turbulent field.

[30] We initially suspected that $\langle E^2 \rangle$ exceeds E_0 because PIC particle noise contributes energy over a large range of short wavelengths. However, in the plane perpendicular to $\vec{B}_0$, the high levels of short-wavelength particle noise do not increase $\langle E^2 \rangle$ substantially. Filtering the 2-D potential, ϕ, data to eliminate waves shorter than 3 m reduces $\langle E \rangle$ by $\sim$ 20%, but this mostly reflects the contribution of waves close to 3 m and not particle fluctuation-dissipation noise. We discuss the implications and possible causes of the high values of $\langle E^2 \rangle$ in the discussion in section 5.

[31] Examining the plasma densities, $n \approx n_e \approx n_i$, gives one a sense of how the turbulence evolves and how it differs in 3-D from 2-D. Figure 2 shows cross-sections of the *B1* densities for a number of times, while Figure 3 shows the same for the equivalent 2-D run. At the earliest time shown for both 3-D and 2-D, one observes waves with a substantially lower amplitude than seen after saturation. This early time allows one to see the underlying particle noise from which the instability grew. Also, short ($\sim$ 3 m) wavelengths dominate the wave structure and both 3-D and 2-D, and show a tilt away from the $\vec{E}\times\vec{B}$ direction resulting from thermal effects [*Oppenheim and Dimant*, 2004; *Dimant and Oppenheim*, 2004]. The 2-D tilts in the opposite direction from that of 3-D because the direction of $\vec{B}_0$ was switched from $\hat{z}$ to $\hat{x}$ for computational reasons. Later in time, in both 3-D and 2-D, longer wavelengths perpendicular to $\vec{B}_0$ begin to predominate over the initial 3 m waves.

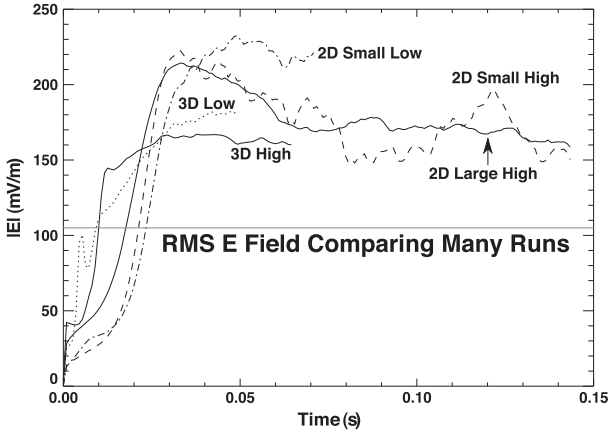

Figure 1. Averaged perturbed global electric field squared $\langle E^2 \rangle$ from a series of comparison 3-D and 2-D runs. "Small" indicates a 512×512 grid size run, while "Large" designates a 2048×2048 case. "Low" designates that $\nu_{e,i}$ were half of the "High" baseline cases.

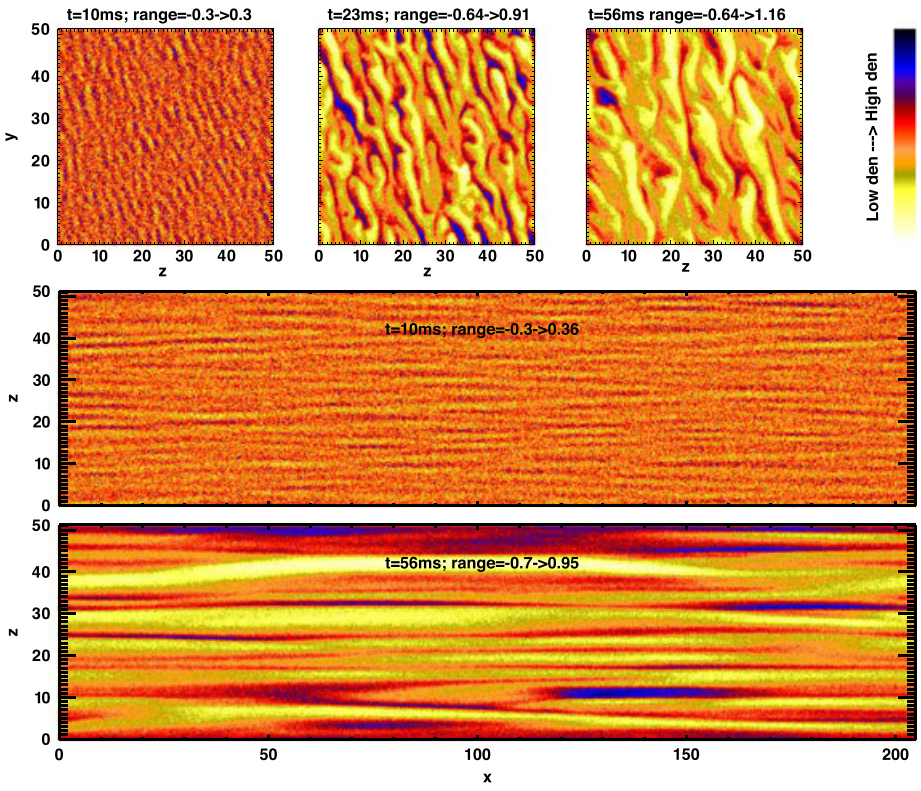

Figure 2. Ion density perturbations during linear growth (t = 10 ms), in transition (t = 23 ms), and in saturation (t = 56 ms). In the simulations, the x direction is along $\vec{B}_0$, while the driving electric field is along y. The top images show cross-sections perpendicular to $\vec{B}_0$, while the lower ones show parallel ones. These densities derive from the cross-sections of the entire 2048 × 512 × 512 mesh. The ranges listed above each image gives the density perturbation of a single cross-section of the simulation. This includes both the wave-induced density perturbations and the not insubstantial particle noise perturbations. The RMS densities give a better indication of density perturbation levels.

[32] In animations of the density cross-sections perpendicular to $\vec{B}_0$, one sees secondary peaks moving along the crests and troughs of the primary waves and perpendicular to their direction of travel. The secondary crest motion goes in the opposite direction from the troughs as described for small 2-D simulations in [*Oppenheim*, 1995]. In the planes parallel to $\vec{B}_0$, perturbations travel rapidly along $\vec{B}_0$ indicative of waves with high parallel group velocities.

[33] Runs in 2-D differ from 3-D ones in that the waves appear sharper. This results from the larger numbers of particles per unit length in these runs. Also, in 2-D, a finite sized box affects the results because of the limited numbers of modes available in the plane perpendicular to $\vec{B}_0$. In 3-D, many slightly oblique modes effectively increase the number of available modes, allowing waves at a broader range of angles to propagate.

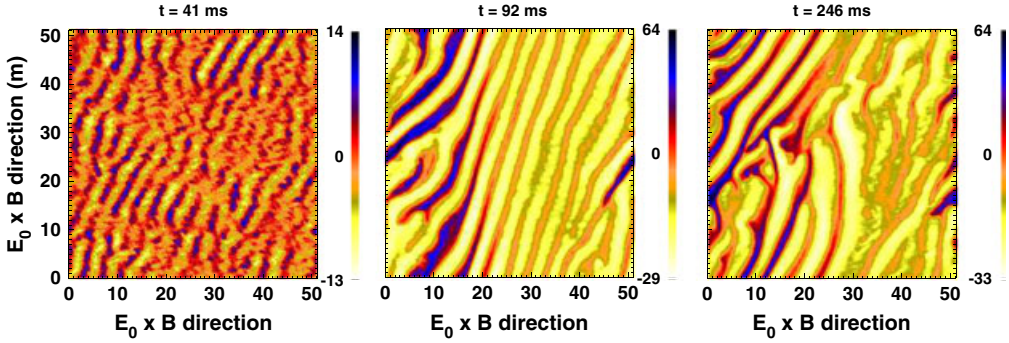

Figure 3. Ion density perturbations during linear growth (t = 41 ms), in transition (t = 92 ms), and in saturation (t = 246 ms) from the *B1* 2-D simulation. These densities derive from the entire particle population distributed over the 512 × 512 mesh. The 2-D simulations grow more slowly, making the times for each stage later than in 3-D.

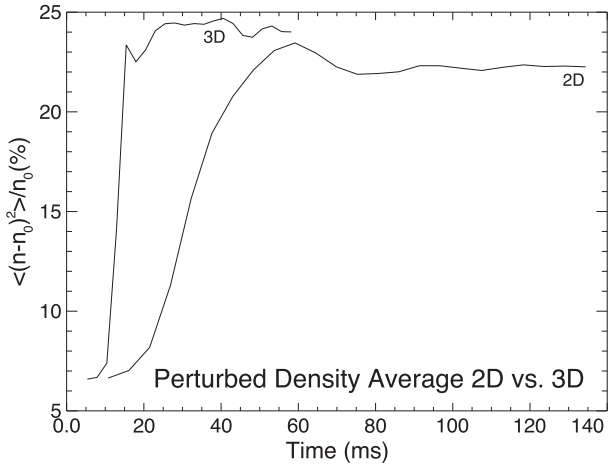

Figure 4. Perturbed density averages versus time for the 3-D and 2-D *B1* simulations. The density values are calculated with $\sqrt{\sum_{\text{all cells}}(\delta n/n_0 - 1)^2/N}$ where N is the number of density values in the simulation.

[34] The higher level of heating in the 3-D simulations has two important effects. First, it reduces turning of the primary waves caused by the thermal instability. Second, it increases the diffusion rate and acoustic speed C_s, which reduces the instability driver's strength and also the saturation level of the wave density perturbations as seen below.

[35] The perturbed density, $\langle \delta n^2 \rangle$, evolution of these simulations tells a similar but not identical story to the field evolution. Figure 4 shows this evolution. As in the electric field evolution plots, the growth rates show that 3-D grows more rapidly than 2-D. Also, the saturation amplitude in 3-D exceeds that in 2-D, although not by a large amount. The cause for this is discussed in section 5.

4.1.1. Temperature Comparisons

[36] As predicted, 3-D Farley-Buneman turbulence heats the electron population dramatically more than 2-D. Figure 5 shows this difference by comparing the moments of the distribution functions in Kelvin. The 2-D electron moment settle at about 1600 K due to a combination of adiabatic wave compression and perpendicular heating, while in 3-D they converge to approximately 2400 K. This 50% increase results from heating by components of the wave-generated electric field parallel to the $\vec{B}_0$, $\delta E_{\parallel}$.

[37] The exact amount of heating depends on the parameters chosen. At higher altitudes in the electrojet, the collision rates drop, and the heating increases. Reducing the simulation collision rate by 2 for both electrons and ions shows a dramatic increase in the temperatures. This corresponds to moving up in altitude about 5.5 km assuming a T_n = 350 K. Figure 6 compares the elevated electron temperatures for a range of collision rates and electric fields.

[38] A series of simulations in which only the length along $\vec{B}_0$ changed shows that the exact $k_{\parallel}$ substantially affects the heating. The *B1* simulation was run for three cases where only the parallel length changed from 100 m to 200 m to 400 m. In the first case, the electron moment reached 2100 K, and in the second it reached 2500 K. The 400 m case was such a large simulation that analyzing it proved difficult. However, the temperature was only a few

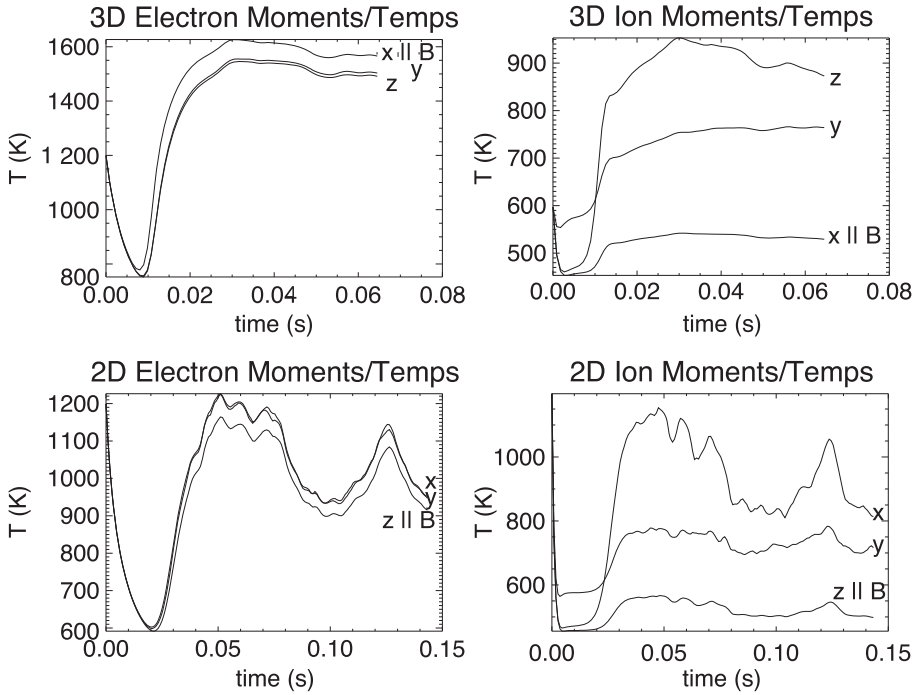

Figure 5. Moments of the electron and ion distributions in 2-D and 3-D from run *B1*. The moments are calculated by summing $(\vec{v} - \vec{v}_0)^2$ over all particles. The lines labeled x, y, or z indicate the component of the velocity summed. Note that in 3-D $\hat{x}$ is parallel to $\vec{B}_0$), while in 2-D $\hat{z}$ is parallel to $\vec{B}_0$. For both 2-D and 3-D, $\vec{E}_0$ points in the $\hat{y}$ direction.

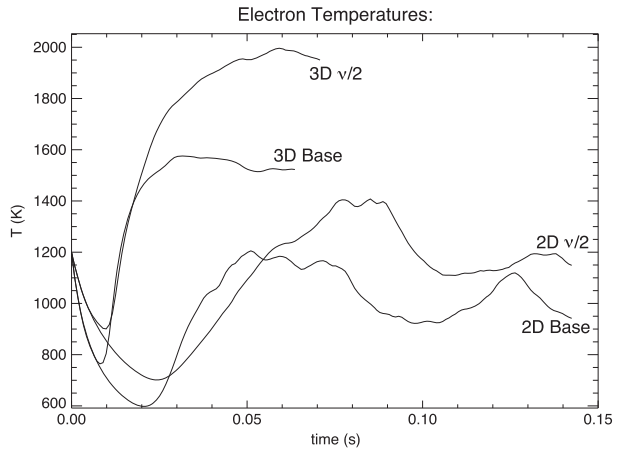

Figure 6. Average electron velocity moments calculated for both 3-D and their comparable 2-D simulations. The 2-D simulations are run for far longer than the 3-D.

percent higher than in the 200 m case. This implies that the heating results from the dynamics of the highly oblique modes, and when the simulation artificially precludes those modes the heating diminishes. Note that these simulations were performed with twice the electron mass of the baseline case, and the $\nu_i \propto v^2 \sim T$ collision algorithm was used instead of the $\nu_i \propto v \sim v_{th}$ one. We assume that a similar scaling occurs for the baseline runs.

4.1.2. Field Comparisons

[39] In order to fully understand the AEH, one needs to know the magnitude of the wave-driven parallel electric fields, $E_\parallel$. The strength of $\langle E_\parallel^2 \rangle$ compared to the total $\langle E^2 \rangle$ reflects the amount of electric field energy in oblique modes and the dominant aspect angle of the system. Figure 7 shows the evolution of this quantity. Initially, $E_\parallel^2$ is 1/3 of E^2 reflecting isotropic noise. As the waves develop, this ratio drops to around 0.045, where it remains relatively constant.

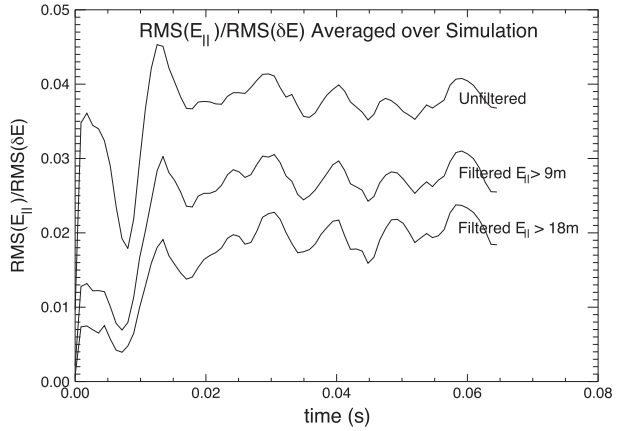

Figure 7. RMS $E_\parallel$ compared with the total RMS E for each time step of the simulation. The top line shows this ratio for unfiltered fields, while the lower lines show it after filtering all parallel modes less than $\sim$ 9 m and $\sim$ 18 m, respectively.

[40] This parallel electric field far exceeds what one expects, given the level of electron heating. A total RMS $\sqrt{\langle E_\parallel^2 \rangle}$ exceeding 20% of the perpendicular RMS field would drive heating electron heating far more heating than necessary to reach 2400 degrees in Figure 5. However, a simple inspection of $E_\parallel$ shows that the parallel field components resulting from the waves only slightly exceeds the noise created by fluctuations of the quasi-random motions of the discrete PIC particles. Hence, $\sqrt{\langle E_\parallel^2 \rangle}$ is dominated by high-frequency noise-generated parallel fields.

[41] Only low-frequency waves drive heating, so we would like to eliminate all high-frequency modes from our calculation of $E_\parallel^2$. However, the simulator only samples the output every 128 time steps to avoid the generation of terabytes of data. Hence, we filtered $\langle E_\parallel^2 \rangle$ only spatially, eliminating parallel waves less than $\sim$ 9 m or $\sim$ 18 m. Unfortunately, this fails to eliminate all high-frequency noise because some aliases into lower frequencies. Fortunately, the fluctuation-dissipation noise is isotropic through $(\vec{k}, \omega)$ space, while the FB-generated parallel fields are predominantly low frequency and long wavelengths. When we filter out all parallel modes less than 9 m long, $E_\parallel^2$ to E^2 ratio drops by a factor of 5, making the RMS $E_\parallel$ less than 10% of E. Even with these filters, this ratio remains elevated because additional, long-wavelength, parallel field noise influences this ratio.

4.2. Pedersen Drift Rates

[42] The simulations show the effects of turbulence on the Pedersen currents. The ion drifts, parallel to $\vec{E}_0$, change only a little in the turbulent system, largely due to ion heating modifying the collision rates. The electron Pedersen drift rates, however, change hugely due to the mechanism discussed in the introduction and, in fact, exceed the ion drifts. Figure 8 shows the electron and ion drifts from the baseline simulations.

[43] In all cases, the drifts grow with the turbulence, overshoot, and then appear to head toward an equilibrium. The

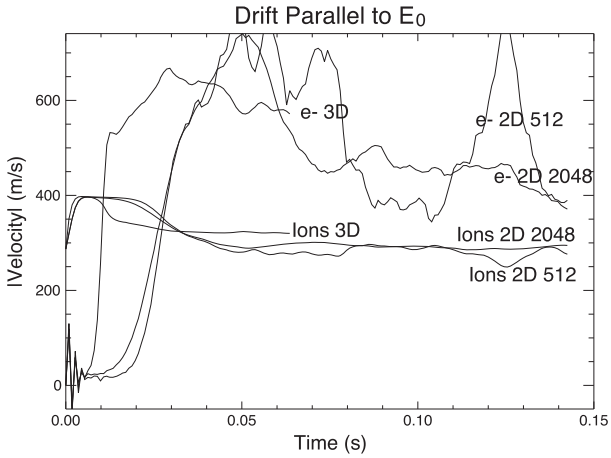

Figure 8. The ion and electron speeds parallel to $\vec{E}_0$ from three baseline runs are compared: 3-D, 2-D (labeled "2D 512"), and the larger 2048 × 2048 2-D (labeled "2D 2048"). The electrons flow in the opposite direction from the ions.

"2D 512" run does not settle within the allotted simulation time, but the "2D 2048" one does. Ideally, we could have run these longer to obtain greater stability, but given the cost of these runs, this was not done. Nevertheless, after the initial overshoot, three interesting features are clear. The anomalous electron drift rate exceeds the ion drift rate by ∼ 85% in 3-D and ∼ 60% in 2-D. Also, the 3-D electron drift rate exceeds the 2-D one by about 1/3, a clear difference.

4.3. Spectra

[44] The density spectra reveal phase velocities, differences between 3-D and 2-D, changes in the FB turbulence as it evolves from the linear growth stage to saturation, and what radars would observe if they measured this type of turbulence. These spectra were generated from the baseline simulations in 2-D and 3-D.

[45] As the system evolves from linearly growing waves to nonlinearly saturated ones, the dominant wavelengths evolve from shorter to longer, and the spectra become more isotropic. Spectra of $E^2(\vec{k}, t)$, shown in Figure 9, reveal that, perpendicular to $\vec{B}$, the initial FB waves grow at limited range of wavelengths with a peak at roughly 3 m. As the system saturates, the dominant modes move to longer wavelength, ranging from 5 m all the way to almost the longest perpendicular size allowed in the system, 50 m. The spectra in the ($x \parallel \vec{B}_0, z \parallel \vec{E}_0 \times \vec{B}_0$) plane shows that initially the waves develop along a line oriented 2.3°off $\vec{B}_0$ with limited spectral width. As the simulation evolves, the spectrum fills in the $k_\parallel$ modes, and the dominant mode moves to longer wavelengths. It also shows relatively little continuing energy at 3 m.

[46] The $\omega - k$ spectra from 3-D simulations show that saturated FB waves have a considerably slower phase velocity than do the 2-D ones despite the elevated 3-D temperatures. Figure 10 shows 3 m and 6 m waves from the saturated second half of each simulation. In 3-D, it shows only the $k_\parallel$ component. Both simulations show that the phase velocity has a cosine-like dependence with respect to the flow angle. However, the phase velocity of the 3-D simulations show a substantially lower peak velocity than do the 2-D ones, roughly 1300 m/s versus 1800 m/s at both 3 m and 6 m.

[47] These spectra also show that the peak spectral power occurs for modes aligned just off perpendicular to $\vec{B}_0$ and falls off for larger Θ (Figure 11). For $\Theta \sim 90°$, the majority of the energy flows in the direction of $\vec{E}_0 \times \vec{B}_0$ (adjusted for the thermal turning effect). As Θ decreases, the energy becomes more isotropic.

5. Discussion

[48] The principal objective of this paper is to present 3-D kinetic simulations of the FB instability, show how this causes anomalous electron heating, and discuss how this relates to theoretical models and observational data showing this heating. Section 4 has shown many aspects of the saturated simulations. The following subsection will discuss the saturated state of the simulated turbulence. Using that result, the next subsection will compare the electron heating observed in the simulations to the heating relatively simple models predict. The last subsection compares the simulations results with predictions of an analytic fluid model.

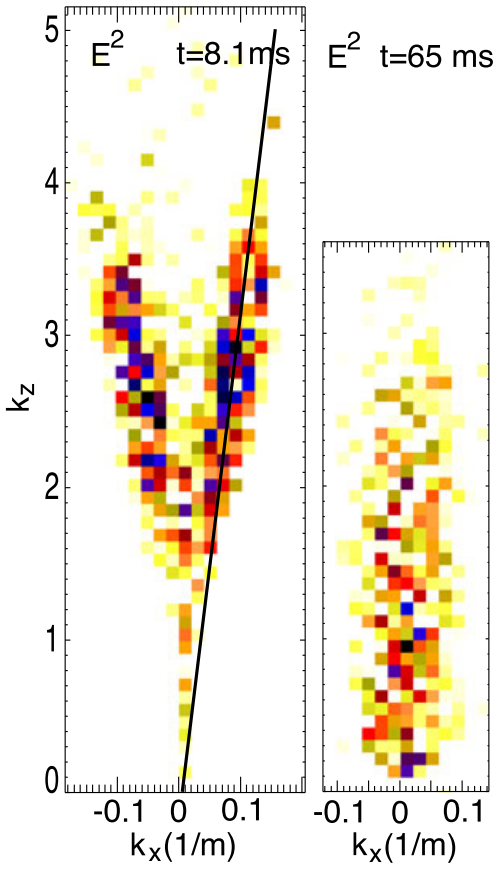

Figure 9. Two snapshots of $E^2(k_x, 0, k_z, t)$ from the *B2* simulation. This shows only the ($x \parallel \vec{B}_0, z \parallel \vec{E}_0 \times \vec{B}_0$)) plane and for $k_y = 0$. Note that the k_x axis goes from –0.2 to 0.2. The maximum spectral energy in the right image increases by a factor of nearly 500 over that in the left one, and the colors scale 2 orders of magnitude in amplitude in a log scale. The line on the left image traces the maximum power lies 2.3 degrees off vertical.

5.1. Analysis of Saturate State

[49] The saturated turbulent electric field in all the simulations (see Figure 1) exceeds the value one would predict theoretically or observationally; see discussion in *Dimant and Milikh* [2003]; *Bahcivan and Cosgrove* [2010]; *Dimant and Oppenheim* [2011b]. The high value of the simulated $\langle \delta \vec{E}^2 \rangle^{1/2}/E_0$ might result from a number of causes: (1) the artificially elevated electron mass used in the simulations causes a nonphysical field; (2) the necessarily finite size of the simulation traps wave energy artificially, elevating the fields; (3) the ion collision model cools the ions somewhat more than in nature; and (4) saturation actually requires a high turbulent field. As discussed below, the evidence points to causes (2) and (3).

[50] The artificial electron mass does not appear to have a major effect on the saturated amplitude of the system. A series of 2-D test runs shows only modest changes in $\langle \delta \vec{E}^2 \rangle$ unless $m_e^{\text{sim}}/m_e \gtrsim 44$. For the baseline 2-D, case $\langle \delta \vec{E}^2 \rangle^{1/2} = 0.165$ for $m_e^{\text{sim}} = 44 m_e$. We also ran many cases with $m_e^{\text{sim}} = 88 m_e$, and this gave $\langle \delta \vec{E}^2 \rangle^{1/2} = 0.22$. A further

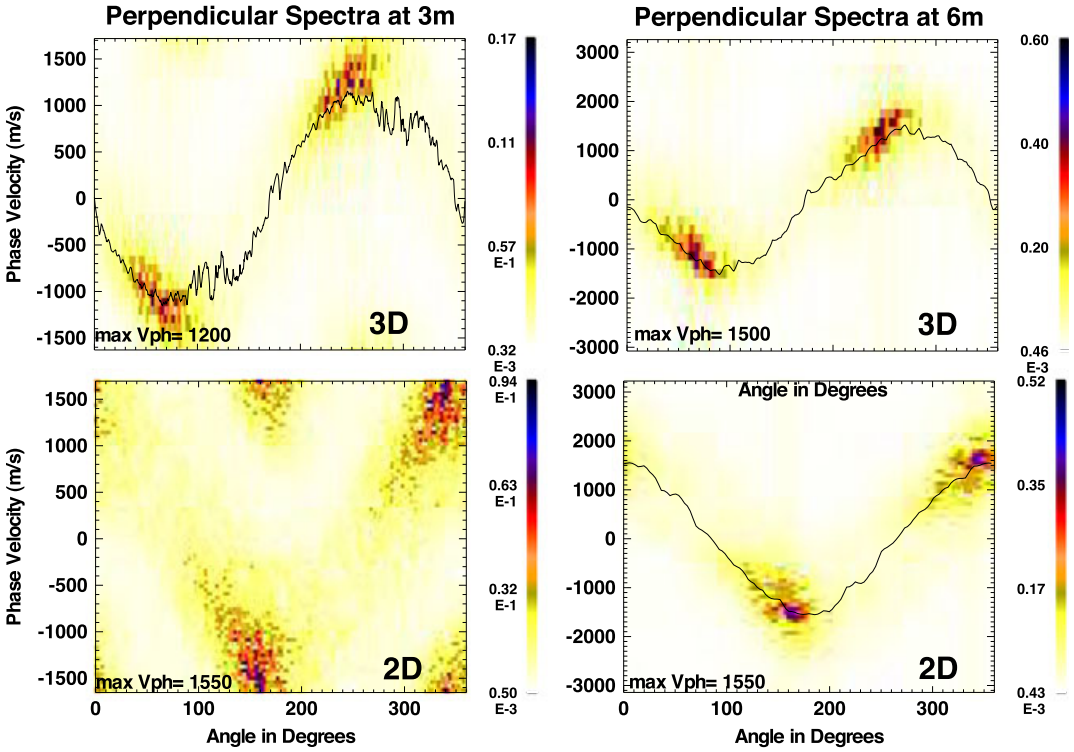

Figure 10. Spectra of 3 m and 6 m waves perpendicular to $\vec{B}_0$ from 3-D and 2-D simulations for the *B2* simulations with double the collision rate and E_0 = 140 mV/m. Generated by taking the second half of the $n_i(x, y, t)$ time sequences from both the 3-D and the 2048 × 2048 2-D simulations, multiplying each time sequence with Hanning window, $h(t)$, and then performing a FFT on $n_i(x, y, t)$*$h(t)$. Linearly interpolating within this data cube to extract all 3 m and 6 m waves and dividing ω by k allows the production of the images. The 2-D simulation has 4 times higher resolution in each perpendicular direction. The black lines show the moment of the distribution which, unfortunately, was affected by aliasing from low phase velocity to high.

test dropped the electron mass by a factor of 4 below the baseline case and gave only a few percent reduction. Hence, we decided the $m_e^{\text{sim}} = 44m_e$ was an acceptable compromise between simulation efficiency and accuracy. Unless a fundamental change occurs when the artificial mass drops below $m_e^{\text{sim}} = 11m_e$, it appears that the chosen m_e^{sim} is not the cause of the high saturated field values.

[51] The simulations clearly show that waves both cascade from the linearly unstable domain to shorter wavelengths and inversely cascade to longer wavelengths. While

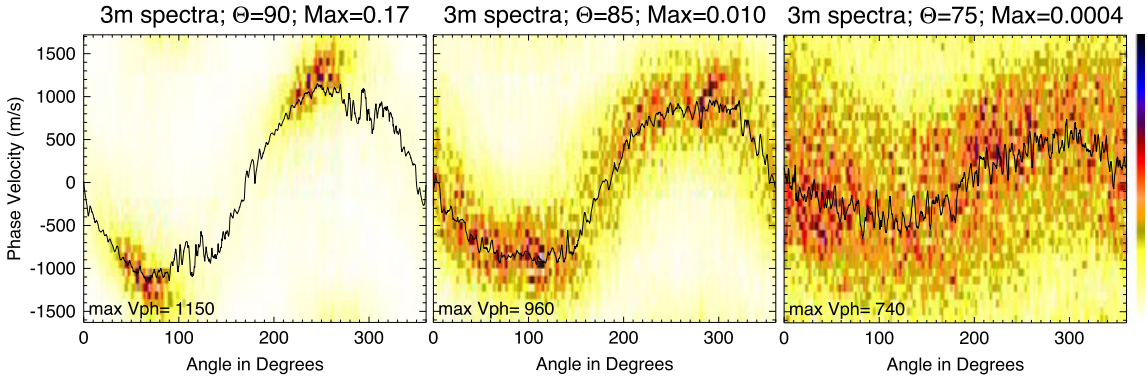

Figure 11. Spectra of 3 m waves at a range of aspect angles Θ from the 3-D *B2* simulation. Generated by taking the second half of the $n_i(x, y, t)$ time sequences from the 3-D, multiplying each time sequence with hanning window, $h(t)$, and then performing a FFT on $n_i(x, y, t)$*$h(t)$. Linearly interpolating within this data cube to extract all 3 m waves and dividing ω by k allows the production of the images. The black lines show the moment of the distribution which, unfortunately, was affected by aliasing from low phase velocity to high.

the simulation models the cascade to shorter wave quite well, the finite box size limits the inverse cascade toward the long-wavelength band. This cascade represents a significant energy flow toward long wavelengths with the spectral-energy maximum reached near the longest wavelengths, Λ, allowed by the simulation box size, $\Lambda \simeq L_{x,y} = L_\perp$. Both our earlier 2-D simulations [*Oppenheim et al.*, 2008] and the current 2-D and 3-D simulations clearly demonstrate this. Also, periodic boundary conditions necessarily restrict wavelengths to discrete modes and completely inhibit waves with $\Lambda > \sqrt{2}L_\perp$. This inhibition cuts off the inverse cascade at the smallest $k_{x,y} = 2\pi/L_\perp$. Unlike the short-wavelength Landau damping, this cutoff includes no wave-energy dissipation and should reflect waves in the $\vec{k}$-space. This leads to the accumulation of the turbulent energy at long wavelengths and may produce larger than expected $\langle \delta \vec{E}^2 \rangle$.

[52] To gain a further insight into this issue, we increased the box size $L_\perp$. The resulting saturated values of $\langle \delta E_\perp^2 \rangle$ remained at similar levels as in the smaller run, as seen in Figure 1. A close look shows the evolution of $\langle E_\perp^2 \rangle^{1/2}$ for both the large and small 2-D runs reaching a maximum of 0.21 mV/m, then dropping over $\sim$ 50 ms to 0.17 mV/m. The smaller run then shows a highly variable $\langle E_\perp^2 \rangle^{1/2}$, while the larger one shows a slow but consistent drop in this value to 0.16 mV/m. This drop may occur as energy pushes to longer wavelengths.

[53] A system where the amplitude of the longest wavelengths continually grows creates an almost intractable problem for simulations. In the FB case, since saturation occurs through coupling to other waves and at the longest wavelengths the simulator may exclude these "other waves," anomalous behaviors may occur. That may lead to excessive fields and heating. However, by showing that the simulations remain largely unchanged as their size increases, we argue that the essential physics at the shorter wavelengths is approximately correct.

[54] As discussed above, the $\nu_i \propto v_i$ ion collision model used does not perfectly match the actual behavior. The ions probably heat more than in our runs, although not as much as in a system which applies a Maxwell-molecule collision model for ions. A 2-D run using a constant ν_i shows increased ion heating, reaching almost 2000 K and hugely non-Maxwellian distribution functions. This increases diffusion and suppresses the instability so that the saturated electric field exceeds the driving field only by about 20%. Due to the cost of the run, no 3-D version of this simulation was done, although we expect a similar reduction in saturated field and increase in ion temperature.

[55] The third possible explanation for the high turbulent electric fields is that they are necessary to saturate the FB system when all other mechanisms are excluded. In the electrojet, inhomogeneities in the plasma densities and conductivities on the kilometer scale size also will play a role in saturating the instability. Plus, the turbulently enhanced conductivities will work to short out the driving electric fields. All these effects would play a role in the natural system.

5.2. Temperature Analysis

[56] This section compares the plasma temperatures predicted by the simulations with a simple two-fluid model described in the appendix. Although pressure gradients and inertia excite the FB instability, this analysis gives an approximate quantitative understanding of temperature without them.

[57] Before analyzing our simulations quantitatively, we will discuss the general kinetic behavior of the plasma. When light electrons collide with heavy neutrals, they scatter over all angles in velocity space much faster than they change their kinetic energy. As a result, the electron velocity distribution, $f_e(\vec{v}_e)$, remains close to isotropic in the neutral frame. This means that a strong parallel electric field, instead of accelerating electrons in the $\vec{B}$-direction, heats them uniformly in all directions. Due to the velocity dependence of the kinetic collision frequency, this heating will also result in deviations from the Maxwellian velocity distribution [*Milikh and Dimant*, 2003]. Despite this, characterizing the electron population with a temperature defined by $T_e \approx (m_e/3) \int f_e v_e^2 d^3 v_e / \int f_e d^3 v_e$ remains adequate. Its averaged value, $\langle T_e \rangle$, is given by equation (A3).

[58] Unlike for electrons, the ion drift velocity is not small compared to the ion thermal speed. Since the magnitude of the imposed E-field in our study exceeds the FB instability threshold, one might expect almost the entire ion population to be shifted in the neutral frame by the suprathermal speed, $v_i \approx eE_0/(m_i \nu_i)$. This does not happen because, according to (A5), the same field $\vec{E}_0$ heats the ions, maintaining a subsonic drift speed. Ultimately, the ions develop a highly anisotropic and nonthermal distribution function $f_i(\vec{v}_i)$ which we will not analyze here.

[59] Simple heating arguments explain the elevated perpendicular ion temperatures seen in Figure 5. Given an E_0 = 105 mV/m field in the $\hat{y}$ direction, equations (A3)–(A5) with $\langle E_\perp^2 \rangle = E_0^2$ and $\langle E_\parallel^2 \rangle = 0$ predict that $T_i \simeq 3T_0 = 900$ K. However, the ion temperatures observed in all runs were noticeably larger. This means that turbulent fields in the perpendicular to $\vec{B}$ direction, $\delta \vec{E}_\perp$, added additional anomalous heating. This might be expected because in these simulations the RMS turbulent field $\langle \delta \vec{E}_\perp^2 \rangle^{1/2}$ always exceeded the driving field. Inserting the observed total average fields into (A3) and (A4) gives much better agreement with the observed temperatures.

[60] In the 3-D runs, the largest ion temperatures were reached in the directions perpendicular to $\vec{B}$, while along $\vec{B}$ the temperature remains much colder. The small parallel field $\vec{E}_\parallel$ does not substantially heat the ions, while the perpendicular fields, $\vec{E}_0$ and $\delta \vec{E}$ will heat the ions in the perpendicular direction. Angular scattering of the ions will then transfer energy from perpendicular to parallel but not rapidly enough to generate isotropic ion temperatures. The cause of the temperature difference in the two perpendicular directions is less obvious, although it most likely results from heating by the turbulent field, $\langle \delta \vec{E}^2 \rangle^{1/2}$, which exceeds the driving field E_0 by a factor of 1.5–2.5 and points mostly in the $\vec{E} \times \vec{B}$ direction.

[61] To estimate the expected levels of plasma heating, we will disregard such complications as anisotropic and non-Maxwellian velocity distributions. Considering a homogeneous ionosphere with the total field $\vec{E} = \vec{E}_0 + \delta \vec{E}$ saturated at a given average level of $\langle E^2 \rangle = E_0^2 + \langle \delta \vec{E}^2 \rangle$, we will estimate average isotropic effective plasma temperatures,

$\langle T_{e,i}\rangle \equiv (m_{e,i}/3)\int f_{e,i}(\vec{v}_{e,i}-\vec{V}_{e,i})^2 d^3v_{e,i}/\int f_{e,i}d^3v_{e,i}$, using the fluid equations (A3)–(A5).

[62] As an example, we analyze "high-altitude" runs with the parameters described in Table 1. For these runs, we have $\nu_{e0} \approx 300\ s^{-1}$, $\nu_{i0} \approx 320\ s^{-1}$, $\kappa_{e0} \approx 670$, $\kappa_{i0} \approx 0.5$, $\Psi_{\perp 0} \approx 3\times 10^{-3}$, and the characteristic aspect angle of FB turbulence (see below) $\Theta_0 \approx 2.7\times 10^{-2} \approx 1.6°$. The value of the undisturbed $\Psi_{\perp 0}$ in the high-latitude ionosphere roughly corresponds to the 112 km altitude [*Dimant and Oppenheim*, 2004, Figure 2]. Combining these parameters with an electric field of $E_0 = 105$ mV/m means that equations (A3)–(A5) with $\langle E_\perp^2\rangle = E_0^2$ and $\langle E_\parallel^2\rangle = 0$ predicts modest temperature elevations of $T_e \simeq 1.35T_0 = 400$ K and $T_i \simeq 3T_0 = 900$ K. However, the steady state temperatures observed even in the 2-D runs were noticeably larger, as seen in Figure 5, due to anomalous heating.

[63] To estimate the turbulent temperatures, one must account for the temperature dependencies of the collision frequencies, $\nu_e \propto \langle T_e\rangle$ and $\nu_i \propto (\langle T_i\rangle + T_0)^{1/2}$. Taking the temperatures directly from simulations (Figure 1), $\langle T_e\rangle \approx 2000$ K and $\langle T_i\rangle \approx 1300$ K, one obtains $\nu_e \approx 2000\ s^{-1}$, $\nu_i \approx 520 s^{-1}$, $\Psi_\perp \approx 3.24\times 10^{-2}$, and $\Theta_0 \equiv [m_e\nu_e/(m_i\nu_i)]^{1/2} \approx 5.5\times 10^{-2} \approx 3.2°$. The highly elevated value of the "heated" $\Psi_\perp \simeq 10\Psi_{\perp 0}$ effectively lowers the altitude roughly by 8 km. This increases the FB threshold field [*Dimant and Milikh*, 2003, equations (14)–(15)] to $E_{\rm Thr} \simeq 60$ mV/m. If nonlinearly saturated turbulence developed according to the model by *Dimant and Milikh* [2003], then we would expect $\langle \delta E_\perp^2\rangle = \alpha_1(45\ \text{mV/m})^2$, where α_1 [*Dimant and Milikh*, 2003, equation (25)] is a factor of order unity. In *Dimant and Milikh* [2003], this factor was tentatively set $\alpha_1 = 1$, but direct comparison with our 3-D simulation shown in Figure 1 yields a much higher value of $\alpha_1 \simeq 10$. The 2-D simulation gives an even larger $\alpha_1 \simeq 15$. At this moment, we just have to accept this disagreement.

[64] Analyzing the turbulent state further requires estimates of the mean particle drifts and how they would be affected by the full heating. In the undisturbed and initially cold ionosphere, one expects an electron Hall speed of $V_{e\rm H} \approx V_{\rm dr} = 2.1$ km/s and a Pedersen speed or $V_{e\rm P} \approx 3$ m/s, although this is poorly resolved. Equation (A2) predicts laminar ion speeds of $V_{i\rm H} \approx 420$ m/s and $V_{i\rm P} \approx 840$ m/s. In the fully heated ionosphere, $V_{e\rm H}$ and $V_{e\rm P}$ should stay essentially the same while the drifts drop to $V_{i\rm H} \approx 180$ m/s and $V_{e\rm P} \approx 590$ m/s.

[65] Equation (A3) predicts the saturated temperatures assuming an average turbulent electric field amplitude. Applying the values of $\sqrt{\langle E_\perp^2\rangle} \approx 0.15$ from Figure 1, $\langle\sqrt{(E_\parallel^2}\rangle/\langle E_\perp^2\rangle) \approx 0.02$ from the filtered (> 18 m) values in Figure 7, and the $E_{\rm min} = 20$ mV/m, one obtains $\langle T_e\rangle \approx 1500$ K. Using the (> 9 m) fitted value of $\langle\sqrt{(E_\parallel^2}\rangle/\langle E_\perp^2\rangle) \approx 0.0275$ gives a $\langle T_e\rangle \approx 2200$ K. The simulation results shown in Figure 6 agree with these values to reasonable accuracy.

5.3. Conductances

[66] Turbulence modifies the conductance of the electrojet with important consequences for the Magnetosphere-Ionosphere (MI) system [*Dimant and Oppenheim*, 2011a, 2011b]. Two mechanisms increase the conductance. First, electron heating reduces the recombination rate which increases the plasma density, increasing the conductivity. This slow process was not modeled in these simulations. Second, the FB instability drives nonlinear electron currents, principally along $\vec{E}_0$ [*Oppenheim*, 1997; *Dimant and Oppenheim*, 2011a]. In our simulations, $\langle\vec{V}_{e\rm P}\rangle \approx \langle\delta n_e\delta\vec{V}_{e\rm P}\rangle/\langle n_e\rangle$ reached hundreds of meters per second, orders of magnitude larger than " heated laminar" $\vec{V}_{e\rm P}$. This contributes substantially to the total Pedersen conductance of the high-latitude ionosphere. The 3-D simulations show a Pedersen current increased by a factor of around 2.8, carried by the electron nonlinear current.

6. Conclusions

[67] The simulations presented in this paper are the first 3-D simulations of the FB instability and show many features observed in the natural ionosphere. In addition to what 2-D turbulence simulations show, these 3-D runs develop small parallel E-fields that heat the electrons. These drive AEH at a level sufficient to explain the auroral heating shown in *Foster and Erickson* [2000]. They also exhibit spectral features compatible with observations. The importance of this study may arise principally from the anomalous conductivity that this turbulence generates, both from the nonlinear transport (or NC) and from the recombination driven by the AEH.

Appendix A: Drift and Temperature Estimates

[68] This Appendix provides simplest two-fluid expressions for the mean particle drift velocities and steady state average plasma temperatures in the highly collisional E region plasma ($\kappa_e \equiv \Omega_e/\nu_e \gg 1$, $\kappa_i \equiv \Omega_i/\nu_i \lesssim 1$). Section 5 compares the simulation results to these simple estimates and discusses possible causes of the differences. In all the equations below, we presume a total electric field, $\vec{E} = \vec{E}_0 + \delta\vec{E}$, where $\vec{E}_0$ is the DC driving field and $\delta\vec{E}$ is a given turbulent field—not necessarily small.

[69] When particle inertia and pressure gradients are neglected, the mean fluid velocity of magnetized electrons ($\Omega_e \gg \nu_e$) is

$$\vec{V}_e = \vec{V}_{e\rm H} + \vec{V}_{e\rm P} + \vec{V}_{e\parallel} \approx \frac{e\vec{E}\times\hat{b}}{m_e\Omega_e} - \frac{e\vec{E}_\perp\nu_e}{m_e\Omega_e^2} - \frac{e\vec{E}_\parallel}{m_e\nu_e}, \qquad \text{(A1)}$$

where $\hat{b} \equiv \vec{B}/B$ and the subscripts $\perp$, $\parallel$ refer to the vector components perpendicular and parallel to $\vec{B}$, respectively. The first (Hall) term in the RHS of (A1) is the $\vec{E}\times\vec{B}$ drift velocity, $\vec{V}_{\rm dr} = \vec{E}\times\vec{B}/B^2$, written in an alternative form for easier comparison with the other terms. The second term, $\vec{V}_{e\rm P} \parallel \vec{E}_\perp$ with $V_{e\rm P} \equiv |\vec{V}_{e\rm P}| = V_{\rm dr}/\kappa_e$ ($V_{\rm dr} \equiv E/B$), describes the much slower Pedersen drift. The third term describes the parallel velocity, $\vec{V}_{e\parallel} \parallel \vec{B}$. In FB turbulence, the parallel field $\vec{E}_\parallel$ is always small, $|\vec{E}_\parallel| \ll |\vec{E}_\perp|$, but the high electron mobility along $\vec{B}$ can give rise to significant $\vec{V}_{e\parallel}$.

[70] The mean fluid velocity of partially unmagnetized ions is given by [e.g., *Dimant and Oppenheim*, 2004, equation (8)]

$$\vec{V}_i = \vec{V}_{i\mathrm{P}} + \vec{V}_{i\mathrm{H}} + \vec{V}_{i\|} = \left(\frac{e\vec{E}}{m_i \nu_i} + \kappa_i^2 \vec{V}_{\mathrm{dr}} \right) \Big/ \left(1 + \kappa_i^2\right). \qquad \text{(A2)}$$

Here the term parallel to $\vec{E}$ describes the ion Pedersen drift, $V_{i\mathrm{P}} \equiv |V_{i\mathrm{P}}| = \kappa_i V_{\mathrm{dr}} / \left(1 + \kappa_i^2\right)$, appended by a relatively small $\vec{V}_{i\|}$. For $\kappa_i \ll 1$, the latter is described by $\vec{E}_\|$ included in $\vec{E}$. We extrapolate this to larger $\kappa_i \lesssim 1$ because for $|\vec{E}_\|| \ll |\vec{E}_\perp|$ slightly different ion responses to $\vec{E}_\|$ and $\vec{E}_\perp$ are inconsequential. The term parallel to $\vec{V}_{\mathrm{dr}}$ (i.e., $\perp \vec{E}_\perp$) describes the ion Hall drift with $|V_{i\mathrm{H}}| = \kappa_i V_{i\mathrm{P}}$.

[71] To calculate spatially temporally averaged electron and ion temperatures, $\langle T_{e,i} \rangle$, the simplest model balances the average frictional heating, $m_s \nu_s \langle V_s^2 \rangle$, against collisional cooling, $(3/2)\delta_{sn}\nu_s(T_0 - \langle T_s \rangle)$, where $\delta_{in} = 1$ for ions and $\delta_{en} \ll 1$ is the mean fraction of energy lost during one inelastic *e-n* collision [*Gurevich*, 1978; *Schunk and Nagy*, 2009]. For the following estimates, we presume that, in the absence of an electric field, all particles have a common cold temperature, $T_0 = T_n$ (in our simulations, $T_0 = 300$ K).

[72] In our simulations, we mimic inelastic losses of electron energy by using an elastic collision model with an artificially reduced neutral mass $m_n = m_{n:e}^{\mathrm{sim}}$. This changes the elastic $\delta_{en} = 2m_e/m_n$ into $\delta_{en}^{\mathrm{sim}} = 2m_e^{\mathrm{sim}}/m_{n:e}^{\mathrm{sim}}$ yielding

$$\langle T_e \rangle = \left[1 + \frac{2}{3} \left(\frac{m_{n:e}^{\mathrm{sim}}}{m_i} \right) \frac{\langle E_\perp^2 \rangle + \kappa_e^2 \langle E_\|^2 \rangle}{E_{\mathrm{min}}^2} \right] T_0, \qquad \text{(A3)}$$

where $E_{\mathrm{min}} = (2T_0/m_i)^{1/2} B \approx 20\,\mathrm{mV/m}$ is the absolute minimum of the FB threshold field and in our simulations $m_{n:e}^{\mathrm{sim}}/m_i = 0.02$. In either the laminar or turbulent *E* region, we always have $\langle E_\|^2 \rangle \ll \langle E_\perp^2 \rangle$, but due to the large multiplier κ_e^2, even small $\langle E_\|^2 \rangle$ can lead to significant electron heating.

[73] The steady state ion temperature, $\langle T_i \rangle$, is [*Dimant and Milikh*, 2003, equation (35)]

$$\langle T_i \rangle = \left[1 + \frac{2}{3} \left(\frac{\kappa_i^2}{1 + \kappa_i^2} \right) \frac{\langle E^2 \rangle}{E_{\mathrm{min}}^2} \right] T_0. \qquad \text{(A4)}$$

Since in most of our simulations the EPPIC collisional algorithm mimicked hard-sphere *i-n* collisions with $\nu_i \propto (T_i + T_0)^{1/2}$, the magnetization parameter $\kappa_i = \Omega_i/\nu_i$ is temperature dependent: $\kappa_i = [2T_0/(\langle T_i \rangle + T_0)]^{-1/2} \kappa_{i0}$, where κ_{i0} is the cold-plasma value of κ_i. For this $\kappa_i(\langle T_i \rangle)$, the implicit relation (A4) reduces to a quadratic equation for $\langle T_i \rangle$ with the unique positive solution:

$$\langle T_i \rangle = \left\{ \left[\left(1 + \kappa_{i0}^2\right)^2 + \frac{4\kappa_{i0}^2}{3} \frac{\langle E^2 \rangle}{E_{\mathrm{min}}^2} \right]^{1/2} - \kappa_{i0}^2 \right\} T_0. \qquad \text{(A5)}$$

For $\kappa_{i0}^2 \langle E^2 \rangle / E_{\mathrm{min}}^2 \ll 1$, equation (A5) reduces to (A4) with constant $\kappa_i = \kappa_{i0}$. In the opposite limit of $\kappa_{i0}^2 \langle E^2 \rangle / E_{\mathrm{min}}^2 \gg 1$, the ion temperature grows linearly with the RMS field, $\langle T_i \rangle \approx 1.15 \kappa_{i0} \langle E^2 \rangle^{1/2} T_0 / E_{\mathrm{min}}$.

[74] **Acknowledgments.** This work was supported by NSF through Ionospheric Physics Grants Nos. ATM-0442075, ATM-0819914, and ATM-1007789; by NASA LWS grant NNX11AO96G; and TeraGrid resources provided by NICS under grant numbers TG-ATM100026 and TG-ATM110034.

References

Bahcivan, H. (2007), Plasma wave heating during extreme electric fields in the high-latitude *E* region, *Geophys. Res. Lett.*, *34*, 15,106–+, doi:10.1029/2006GL029236.

Bahcivan, H., and R. Cosgrove (2010), On the generation of large wave parallel electric fields responsible for electron heating in the high-latitude *E* region, *J. Geophys. Res. Space Phys.*, *115*(A14), A10304, doi:10.1029/2010JA015424.

Bahcivan, H., R. B. Cosgrove, and R. T. Tsunoda (2006), Parallel electron streaming in the high-latitude *E* region and its effect on the incoherent scatter spectrum, *J. Geophys. Res.*, *111*, doi:10.1029/2005JA011,595.

Bahcivan, H., J. W. Cutler, M. Bennett, B. Kempke, J. C. Springmann, J. Buonocore, M. Nicolls, and R. Doe (2012), First measurements of radar coherent scatter by the Radio Aurora Explorer CubeSat, *Geophys. Res. Lett.*, *L14101*, doi:10.1029/2012GL052249.

Bowles, K. L. (1954), Doppler-shifted radio echoes from Aurora, *J. Geophys. Res.*, *59*, 553.

Buchert, S. C., T. Hagfors, and J. F. McKenzie (2006), Effect of electrojet irregularities on DC current flow, *J. Geophys. Res.*, *111*(A10), A02305, doi:10.1029/2004JA010788.

Dimant, Y. S. (2000), Nonlinearly saturated dynamical state of a three-wave mode-coupled dissipative system with linear instability, *Phys. Rev. Lett.*, *84*, 622–625.

Dimant, Y. S., and G. M. Milikh (2003), Model of anomalous electron heating in the *E* region: 1. Basic theory, *J. Geophys. Res.*, *108*, 5–1, doi:10.1029/2002JA009524.

Dimant, Y. S., and M. M. Oppenheim (2004), Ion thermal effects on *E*-region instabilities: Linear theory, *J. Atmos. & Solar Terr. Phys.*, *66*, 1655–1668.

Dimant, Y. S., and M. M. Oppenheim (2011a), Magnetosphere-ionosphere coupling through *E*-region turbulence: 1. Energy budget, *J. Geophys. Res.*, *116*(A09), A09,303, doi:10.1029/2011JA016648.

Dimant, Y. S., and M. M. Oppenheim (2011b), Magnetosphere-ionosphere coupling through *E*-region turbulence: 2. Anomalous conductivities and frictional heating, *J. Geophys. Res.*, *116* (A09), A09,304, doi:10.1029/2011JA016649.

Dimant, Y. S., and R. N. Sudan (1995), Kinetic theory of the Farley-Buneman instability in the E region of the ionosphere, *J. Geophys. Res.*, *100*, 14,605–14,624.

Farley, D. T. (1985), Theory of equatorial electrojet plasma waves: New developments and current status, *J. Atmos. Terr. Phys.*, *47*, 729.

Fejer, B. G., J. Providakes, and D. T. Farley (1984), Theory of plasma waves in the auroral E region, *J. Geophys. Res.*, *89*, 7487.

Foster, J. C., and P. J. Erickson (2000), Simultaneous observations of *E*-region coherent backscatter and electric field amplitude at F-region heights with the Millstone Hill UHF radar, *Geophys. Res. Lett.*, *27*, 3177.

Gurevich, A. V. (1978), *Nonlinear Phenomena in the Ionosphere*, Springer Series on Physics Chemistry Space, vol. 10, Springer Verlag.

Haldoupis, C., T. Ogawa, K. Schlegel, J. A. Koehler, and T. Ono (2005), Is there a plasma density gradient role on the generation of short-scale Farley-Buneman waves? *Ann. Geophys.*, *23*, 3323–3337.

Hamza, A. M., and H. Imamura (2001), On the excitation of large aspect angle Farley-Buneman echoes via three-wave coupling: A dynamical system model, *J. Geophys. Res.*, *106*, 24,745–24,754, doi:10.1029/2000JA000065.

Hysell, D. L., and J. Drexler (2006), Polarization of elliptic *E* region plasma irregularities and implications for coherent radar backscatter from Farley-Buneman waves, *Radio Sci.*, *41*, 4015, doi:10.1029/2005RS003424.

Hysell, D. L., J. Drexler, E. B. Shume, J. L. Chau, D. E. Scipion, M. Vlasov, R. Cuevas, and C. Heinselman (2007), Combined radar observations of equatorial electrojet irregularities at Jicamarca, *Ann. Geophys.*, *25*, 457–473.

Kelley, M. C. (2009), *The Earth's Ionosphere: Plasma Physics and Electrodynamics*, Academic Press.

Milikh, G. M, and Y. S Dimant (2003), Model of anomalous electron heating in the *E* region: 2. Detailed numerical modeling, *J. Geophys. Res.*, *108*, 6–1, doi:10.1029/2002JA009527.

Milikh, G. M., L. P. Goncharenko, Y. S. Dimant, J. P. Thayer, and M. A. McCready (2006), Anomalous electron heating and its effect on the elec-

tron density in the auroral electrojet, *Geophys. Res. Lett.*, *33*, 13,809–+, doi:10.1029/2006GL026530.

Oppenheim, M. M. (1995), Nonlinear simulations and theory of the Farley-Buneman instability in the E region ionosphere, Ph.D. thesis, Cornell Univ., Ithaca, N. Y.

Oppenheim, M. M. (1997), Evidence and effects of a wave-driven nonlinear current in the equatorial electrojet, *Ann. Geophys.*, *15*, 899.

Oppenheim, M. M., and Y. S. Dimant (2004), Ion thermal effects on *E*-region instabilities: 2-D kinetic simulations, *J. Atmos. & Solar Terr. Phys.*, *66*, 1639–1654.

Oppenheim, M. M., Y. Dimant, and L. P. Dyrud (2008), Large-scale simulations of 2-D fully kinetic Farley-Buneman turbulence, *Ann. Geophys.*, *26*, 543–553.

Otani, N. F., and M. Oppenheim (2006), Saturation of the Farley-Buneman instability via three-mode coupling, *J. Geophys. Res. Space Phys.*, *111* (A10), 3302, doi:10.1029/2005JA011215.

Providakes, J., D. T. Farley, B. G. Fejer, J. Sahr, and W. E. Swartz (1988), Observations of auroral *E*-region plasma waves and electron heating with EISCAT and a VHF radar interferometer, *J. Atmos. Terr. Phys.*, *50*, 339–347.

Robinson, T. R. (1986), Towards a self-consistent non-linear theory of radar auroral backscatter, *J. Atmos. Terr. Phys.*, *48*, 417.

Robinson, T. R., and F. Honary (1993), Adiabatic and isothermal ion-acoustic speeds of stabilized Farley-Buneman waves in the auroral *E*-region, *J. Atmos. Terr. Phys.*, *55*, 65–77.

Rosenberg, M., and V. W. Chow (1998), Farley-Buneman instability in a dusty plasma, *Planet. Space Sci.*, *46*, 103–108.

Sahr, J. D., and D. T. Farley (1995), Three-wave coupling in the auroral *E*-region, *Ann. Geophys.*, *13*, 38–44.

Schlegel, K., and J. P. St.-Maurice (1981), Anomalous heating of the polar E region by unstable plasma waves, 1, Observations, *J. Geophys. Res.*, *86*, 1447.

Schunk, R. W., and A. F. Nagy (2009), *Ionospheres,* 2nd ed., 628 pp., Cambridge University Press, Cambridge, U. K.

St.-Maurice, J. P (1987), A unified theory of anomalous resistivity and Joule heating effects in the presence of ionospheric E region irregularities, *J. Geophys. Res.*, *92*, 4533.

St.-Maurice, J.-P. (1990), Electron heating by plasma waves in the high latitude *E*-region and related effects: Theory, *Adv. Space Res.*, *10*, 6(239)–6(249).

St.-Maurice, J.-P., and A. M. Hamza (2001), A new nonlinear approach to the theory of *E* region irregularities, *J. Geophys. Research*, *106*, 1751–1760.

St.-Maurice, J.-P., and R. Laher (1985), Are observed broadband plasma wave amplitudes large enough to explain the enhanced electron temperatures of the high-latitude *E* region? *J. Geophys. Research*, *90*, 2843–2850.

St.-Maurice, J.-P., W. Kofman, and E. Kluzek (1990), Electron heating by plasma waves in the high latitude *E*-region and related effects: Observations, *Adv. Space Res.*, *10*, 6(225)–6(237).

Stauning, P., and J. K. Olesen (1989), Observations of the unstable plasma in the disturbed polar *E*-region, *Physica Scripta*, *40*, 325–332.

Williams, P. J. S., B. Jones, and G. O. L. Jones (1992), The measured relationship between electric field strength and electron temperature in the auroral *E*-region, *J. Atmos. Terr. Phys.*, *54*, 741–748.

Woodman, R. F., and J. L. Chau (2002), First Jicamarca radar observations of two-stream *E* region irregularities under daytime counter equatorial electrojet conditions, *J. Geophys. Res.*, *107*(A12), 1482, doi: 10.1029/2002JA009362.